

## Separation Membranes

# Multiplying Oxygen Permeability of a Ruddlesden-Popper Oxide by Orientation Control via Magnets

Zhijun Zhao,\* Guoxing Chen, Giamper Escobar Cano, Patrick A. Kießling, Oliver Stöling, Bernd Breidenstein, Sebastian Polarz, Nadja C. Bigall, Anke Weidenkaff, and Armin Feldhoff\*

**Abstract:** Ruddlesden-Popper-type oxides exhibit remarkable chemical stability in comparison to perovskite oxides. However, they display lower oxygen permeability. We present an approach to overcome this trade-off by leveraging the anisotropic properties of  $\text{Nd}_2\text{NiO}_{4+\delta}$ . Its  $(a,b)$ -plane, having oxygen diffusion coefficient and surface exchange coefficient several orders of magnitude higher than its  $c$ -axis, can be aligned perpendicular to the gradient of oxygen partial pressure by a magnetic field (0.81 T). A stable and high oxygen flux of  $1.40 \text{ mL min}^{-1} \text{ cm}^{-2}$  was achieved for at least 120 h at 1223 K by a textured asymmetric disk membrane with 1.0 mm thickness under the pure  $\text{CO}_2$  sweeping. Its excellent operational stability was also verified even at 1023 K in pure  $\text{CO}_2$ . These findings highlight the significant enhancement in oxygen permeation membrane performance achievable by adjusting the grain orientation. Consequently,  $\text{Nd}_2\text{NiO}_{4+\delta}$  emerges as a promising candidate for industrial applications in air separation, syngas production, and  $\text{CO}_2$  capture under harsh conditions.

Oxygen transporting membranes (OTMs), which consist of mixed ionic-electronic conductors (MIECs), can selectively transport oxygen ions and electrons while preventing the passage of other gases. This property makes them suitable for various industrial and environmental applications such as oxygen separation,<sup>[1]</sup>  $\text{CO}_2$  capture and storage,<sup>[2]</sup> solid state fuel cells (SOFCs),<sup>[3]</sup> and membrane reactors.<sup>[4]</sup> Since  $\text{CO}_2$  is often involved in those applications, both high oxygen flux and  $\text{CO}_2$ -tolerance of membranes are required. In an economic perspective, the flux should be greater than  $5 \text{ mL min}^{-1} \text{ cm}^{-2}$ .<sup>[5]</sup>  $\text{Ba}_{0.5}\text{Sr}_{0.5}\text{Co}_{0.8}\text{Fe}_{0.2}\text{O}_{3-\delta}$  has remarkable permeability (approx.  $10 \text{ mL min}^{-1} \text{ cm}^{-2}$  by adopting a hollow-fiber configuration), but its flux diminishes immediately when the atmosphere contains 5%  $\text{CO}_2$  due to the formation of alkaline-earth metal carbonates.<sup>[6]</sup>

Another perovskite family  $\text{RE(TM)O}_3$ , e.g.  $\text{La}_{0.6}\text{Sr}_{0.4}\text{Co}_{0.8}\text{Fe}_{0.2}\text{O}_{3-\delta}$ , shows good  $\text{CO}_2$ -stability due to the incorporation of rare-earth metal (RE), however, with the

compromise of lower flux.<sup>[2b,7]</sup> Introducing asymmetric membrane or hollow-fiber configurations comprising a thin dense layer and a thick porous layer can enhance the flux of  $\text{RE(TM)O}_3$  membranes.<sup>[8]</sup> The porous layer reinforces the mechanical strength of the membrane while also accelerating the surface exchange process. Nevertheless, at this stage, the surface exchange process becomes the limiting step for oxygen permeation, and reducing the membrane thickness further only increases the flux marginally. Coating the membrane surface with MIEC powders, especially at the low oxygen potential side (sweep side), is another approach to expedite the surface exchange process.<sup>[8c,9]</sup> However, it is essential to consider that the coating materials often contain elements such as Sr and Co (e.g.  $\text{La}_{0.6}\text{Sr}_{0.4}\text{CoO}_{3-\delta}$ ), which destabilize in  $\text{CO}_2$  or even in air after long-term storage and adversely impede the oxygen flux.<sup>[8b,9c,10]</sup>

Furthermore, the problem with limited  $\text{CO}_2$ -stability can be overcome by utilizing alkaline-earth-metal-free material,

[\*] Z. Zhao, G. Escobar Cano, P. A. Kießling, Prof. Dr. N. C. Bigall, Prof. Dr. A. Feldhoff  
 Institute of Physical Chemistry and Electrochemistry, Leibniz University Hannover  
 Callinstr. 3A, 30167 Hannover (Germany)  
 E-mail: zhijun.zhao@pci.uni-hannover.de  
 armin.feldhoff@pci.uni-hannover.de

Dr. G. Chen, Prof. Dr. A. Weidenkaff  
 Fraunhofer Research Institution for Materials Recycling and Resource Strategies IWKS  
 Brentanostr. 2a, 63755 Alzenau (Germany)

O. Stöling, Prof. Dr. S. Polarz  
 Institute of Inorganic Chemistry, Leibniz University Hannover  
 Callinstr. 9, 30167 Hannover (Germany)

Prof. Dr. B. Breidenstein  
 Institute of Production Engineering and Machine Tools, Leibniz University Hannover  
 An der Universität 2, 30823 Garbsen (Germany)

Prof. Dr. A. Weidenkaff  
 Department of Materials and Earth Sciences, Technical University Darmstadt  
 Peter-Grünberg-Str. 2, 64287 Darmstadt (Germany)

© 2023 The Authors. Angewandte Chemie International Edition published by Wiley-VCH GmbH. This is an open access article under the terms of the Creative Commons Attribution Non-Commercial NoDerivs License, which permits use and distribution in any medium, provided the original work is properly cited, the use is non-commercial and no modifications or adaptations are made.

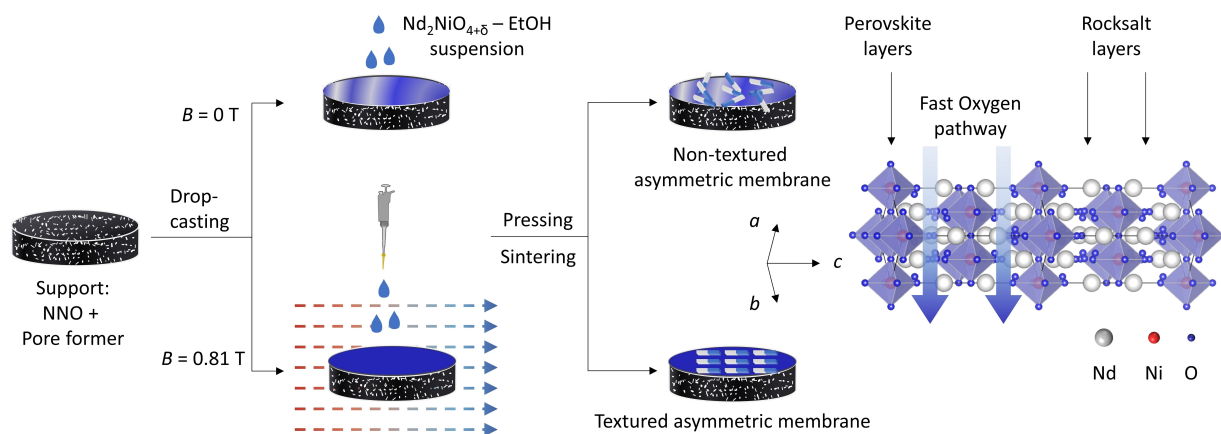


**Figure 1.** Schematic illustration of the membrane preparation.

e.g. the Ruddlesden-Popper phase with  $K_2NiF_4$ -type structure  $Ln_2NiO_{4+\delta}$ , where Ln can be La, Nd, and Pr.<sup>[2b,11]</sup> The structure of lanthanide nickelate is composed of  $LnO$  rock-salt layers and  $LnNiO_3$  perovskite layers alternating along its crystallographic  $c$ -axis (see Figure 1), while the interstitial oxygen species locate in rock-salt layers.<sup>[12]</sup> The bulk diffusion and surface exchange coefficients in the  $(a,b)$ -plane are significantly higher than those along the  $c$ -axis. For  $Nd_2NiO_{4+\delta}$  (NNO) single crystal, the bulk diffusion coefficient in the  $(a,b)$ -plane is nearly three orders of magnitude higher than that along the  $c$ -axis whereas the surface exchange coefficient is more than twice as high at 973 K.<sup>[13]</sup> Comparing the single crystal with polycrystalline NNO, the bulk diffusion coefficient in the  $(a,b)$ -plane at 973 K is more than five times higher.<sup>[11d,13–14]</sup> NNO also shows larger oxygen diffusion coefficient in the  $(a,b)$ -plane than the electrolyte material  $Ce_{0.8}Gd_{0.2}O_{2-\delta}$  and the SOFC cathode material  $La_{0.5}Sr_{0.5}CoO_{3-\delta}$ , being  $4.1 \times 10^{-8} \text{ cm}^2 \text{ s}^{-1}$ ,  $0.7 \times 10^{-8} \text{ cm}^2 \text{ s}^{-1}$ , and  $0.3 \times 10^{-8} \text{ cm}^2 \text{ s}^{-1}$  at 873 K, respectively.<sup>[13,15]</sup>

Despite the outstanding  $CO_2$ -stability and excellent transport properties in its  $(a,b)$ -plane, the oxygen flux of NNO membranes with random grain orientation is lower than currently studied materials. Fortunately, NNO also shows anisotropy in magnetic susceptibility and its easy-magnetization axis is its crystallographic  $c$ -axis.<sup>[16]</sup> For NNO with  $\delta=0.23$ , the susceptibilities parallel and perpendicular to its  $c$ -axis are  $2.430 \times 10^{-3} \text{ cm}^3 \text{ mol}^{-1}$  and  $0.875 \times 10^{-3} \text{ cm}^3 \text{ mol}^{-1}$  at 298 K, respectively.<sup>[17]</sup> The corresponding difference between the molar magnetic susceptibilities is  $1.555 \times 10^{-3} \text{ cm}^3 \text{ mol}^{-1}$ , meaning that it is possible to align NNO particles in a 1 T magnetic field.<sup>[18]</sup> Herein, we report the preparation of textured asymmetric NNO membranes with  $(a,b)$ -planes perpendicular to the gradient of oxygen pressure and its application in oxygen separation in the presence of  $CO_2$ .

As illustrated in Figure 1, a support composed of NNO and a pore-former is placed into the magnetic field (see also Figures S1 and S2). During drop-casting, a textured thin layer is formed on the support. The green body has to be pressed before sintering to ensure the gas-tightness of the membrane (cf. Figure S7).

The phase purity of the powder and texture of membranes were analyzed by X-ray diffraction (XRD) as depicted in Figure 2. The XRD pattern of the powder exhibited distinctive reflections, affirming its pristine phase purity. The observed reflections were assignable to the orthorhombic phase, with an oxygen over-stoichiometry  $\delta$  equal to 0.20 measured by thermogravimetric analysis (see Figure S5). Through drop-casting in a 0.81 T magnetic field, the easy-magnetization axis (i.e.  $c$ -axis) of NNO particles was aligned with the direction of the magnetic field (c.f. Figure 2b,d). The green body showed a preferred orientation along the  $a$ - and  $b$ -axes, as well as the  $(a,b)$ -plane, as evident from the higher intensity of the reflections corresponding to the  $(0k0)$ ,  $(h00)$  and  $(hk0)$  planes. Upon sintering, an amplified textural ordering was discernible, as evident in Figure 2e and Figure S11b,c. We found an irregular distribution of the grains along their  $a$ - and  $b$ -axes by analyzing the reflection intensities in 14 samples as shown in Figure S12. To quantitatively assess this enhanced texture,

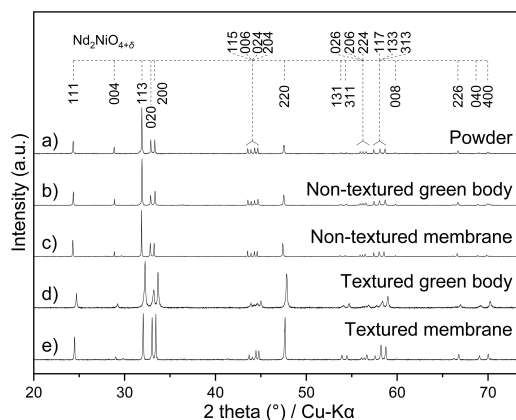


**Figure 2.** XRD patterns of  $Nd_2NiO_{4+\delta}$  a) powder, non-textured b) green body and c) membrane, textured d) green body and e) membrane. The reflections involved in calculating of Lotgering factor are indexed using the standard pattern of orthorhombic  $Nd_2NiO_{4+\delta}$  (ICSD collection code: 50440). The XRD data are normalized to the same height of the 113 reflection.

the Lotgering factor, which ranges from 0 for random orientation to 1 for perfect orientation,<sup>[19b]</sup> was calculated by Equation S7 (see Support Information) using the reflection intensities listed in Table S1. The green bodies exhibited Lotgering factors of 0 for the non-textured variant and 0.25 for the textured counterpart, while the sintered membranes are 0.03 and 0.31, respectively. The enhancement indicates that the sintering process facilitates the formation of a preferred orientation in the NNO samples. The phenomenon can be explained by the thermal motion during drop-casting and the Ostwald ripening during sintering. Magnetic torque aligns large particles during casting, while smaller ones (e.g. < 100 nm, see Figure S4b) remain random due to the dominate thermal motion as indicated by Equation S2.<sup>[19c]</sup> Sintering then causes large oriented particles to consume smaller ones, increasing orientation degree. The phenomenon is also observed in ceramics of other oxides processed in magnetic fields.<sup>[19]</sup>

The texture of membranes was further analyzed by XRD pole figures, focusing on the (004), (113), and (220) planes, as depicted in Figure 3. Pole figures for the (020) and (200) planes were not conducted due to the limitations of the point focus technique, which has low angular resolution and does not allow for the separation of these two reflections. While the (004) and (113) pole figures showed a slightly lower intensity in the textured membrane compared with the non-textured counterpart, the (220) pole figure of the textured membrane demonstrated a more concentrated intensity. The multiples of a random distribution (MRD) were calculated based on the estimated orientation density function data to quantitatively evaluate the level of texture. MRD values range from 1 for a non-textured sample to infinity for a single crystal, representing the degree of preferred orientation within a sample. Consistent with the Lotgering factors determined from Figure 2, the membrane prepared under the assistance of a magnetic field exhibited a preferred orientation within the (*a,b*)-plane. It had an MRD of 5.6, higher than the membrane prepared without using the magnetic field.

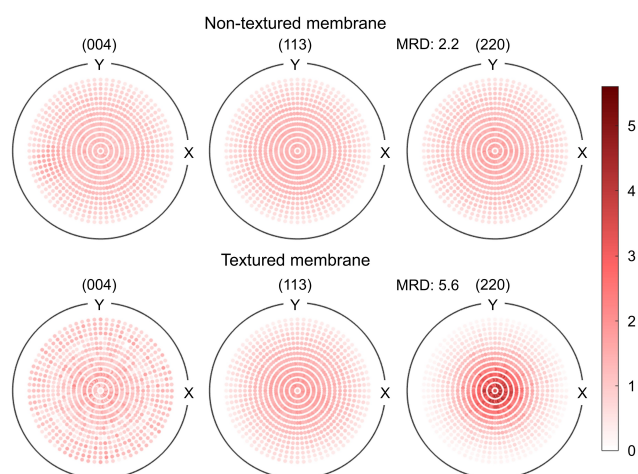


**Figure 3.** XRD pole figures of  $\text{Nd}_2\text{NiO}_{4+\delta}$  non-textured and textured membranes. MRD stands for multiples of a random distribution.

The morphology of the green body after drop-casting and the membranes after sintering is illustrated in Figure S7. The drop-cast layer on the green body exhibited numerous pores. When the drop-cast layer was sintered directly without pressing, a porous membrane was produced, as shown in Figure S7c,d. This can be attributed to insufficient particle contact prior to reaching the sintering temperature. As depicted in Figure 4, the layer became denser after the green body was pressed and sintered, regardless of whether the drop-cast layer was prepared outside or inside a magnetic field. Additional top-view and cross-sectional views can be observed in Figure S7e–g, providing a broader perspective at lower magnifications. In agreement with SEM images, the results of mercury porosimetry analysis revealed that the not-pressed membrane had a broad distribution of pore diameter with an average value of  $12.5\ \mu\text{m}$ , whereas the pressed membrane did not exhibit macropores (Figure S8). The grain size distribution of the textured and non-textured membranes was deduced from SEM images and represented as histograms, which were further fitted with a log-normal distribution (Figure S13). The average size of the textured and non-textured membranes was quite similar, measuring approximately  $9.90 \pm 0.51\ \mu\text{m}$  and  $9.65 \pm 0.10\ \mu\text{m}$ , respectively.

The influence of membrane configurations (both symmetric and asymmetric) and grain orientation on the oxygen flux was investigated. A comprehensive investigation is presented in Figures S16–S20. Figure 5a illustrates the relationship between the flux and temperature for NNO membranes with different thicknesses of the dense layer, where the total thickness of all membranes was kept at 1.0 mm. As discussed earlier, a magnetic field of 0.81 T can orient the *c*-axis of NNO particles along the direction of the magnetic field. Although subsequent pressing weakens the particle orientation as displayed in Figure S9, the sintering process can partially recover the orientation. After polishing

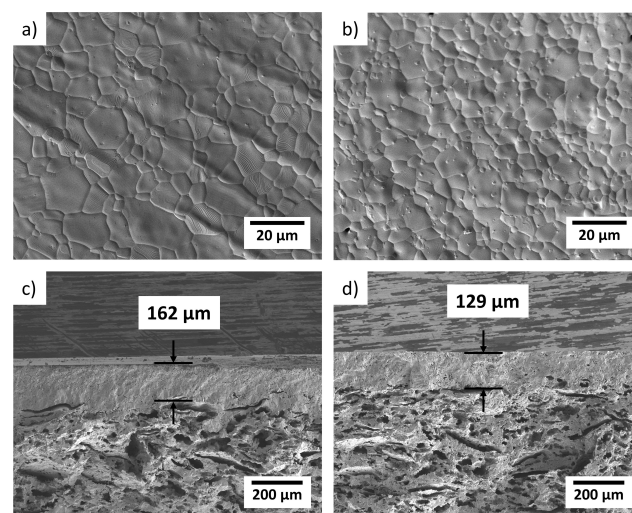


**Figure 4.** SEM images of  $\text{Nd}_2\text{NiO}_{4+\delta}$  asymmetric membrane prepared a), c) inside a 0.81 T magnetic field, and b), d) outside the magnetic field. The lines in a) and b) originated from a die during the pressing process.

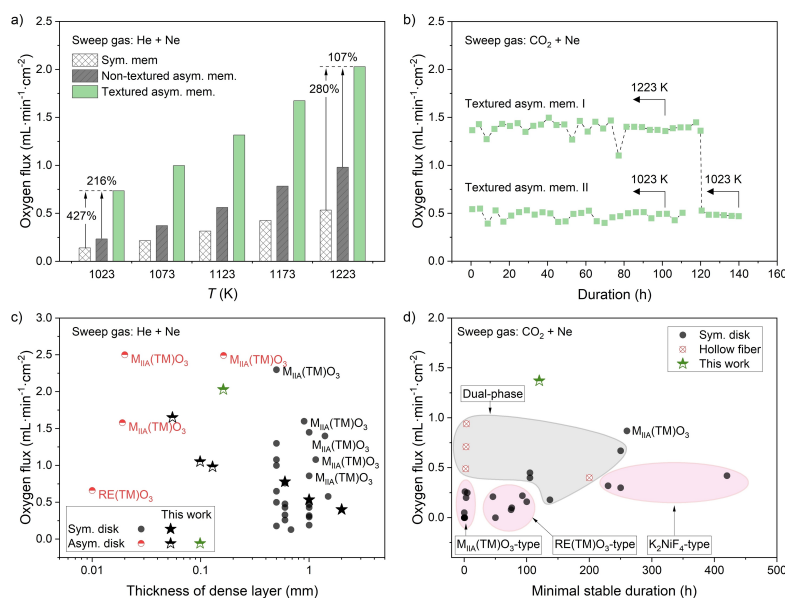


**Figure 5.** a) Oxygen flux of symmetric, non-textured asymmetric, and textured asymmetric membranes in air/He gradient as a function of temperature. All membranes have a total thickness of 1 mm, while the thicknesses of the dense layer are 0.129 mm for the non-textured membrane and 0.162 mm for the textured membrane. b) Long-term stability test of textured asymmetric membranes in air/CO<sub>2</sub> gradient at 1223 K and 1023 K. The thicknesses of the dense layer are 0.162 mm and 0.145 mm for membrane I and membrane II, respectively. c) Comparison of oxygen flux of various membranes at 1223 K as a function of dense layer thickness. d) Comparison of CO<sub>2</sub>-stability of various membranes at 1223 K. Information on the data points is listed in Supporting Information Table S3.

the dense layer, the Lotgering factor remained almost unchanged (Figure S10), indicating consistent particle orientation in the direction of the layer thickness. The membrane used for oxygen permeation testing had a Lotgering factor of 0.36 and a dense layer thickness of 162 μm. Despite the dense layer of the textured membrane being 26% thicker than the non-textured membrane (cf. Figure 4c,d), it still exhibited the highest flux across the measured temperature range as shown in Figure 5a: 0.74 mL min<sup>-1</sup> cm<sup>-2</sup> at 1023 K and 2.03 mL min<sup>-1</sup> cm<sup>-2</sup> at 1223 K, representing 216% and 107% improvement compared to the non-textured membrane, respectively. Further improvement is expected with equal dense layer thickness of textured and non-textured membranes. The enhancement in the low-temperature range compared to the high-temperature range supports the conclusion deduced from Figure S19 that the oxygen transport in NNO is predominately controlled by surface exchange at 1023 K and bulk diffusion at 1223 K.

Table S2 summarizes the bulk diffusion coefficients and surface exchange coefficients of NNO single crystals and polycrystalline bulks at 973 K as reported in the literature.<sup>[11d,13–14,20]</sup> At this temperature, the bulk diffusion coefficient in the (*a,b*)-plane is 3.8–5.3 times higher for single crystals compared to polycrystalline materials (i.e. randomly oriented), while the surface exchange coefficient in the (*a,b*)-plane is 2.6–16.9 times higher for single crystals. It is worth noting that in terms of Lotgering factor and MRD value, the orientation degree of this membrane is only moderate and is not as high as the ceramics prepared by Murata et al.<sup>[16]</sup> This is partly due to the weakening of

orientation during the pressing process (which is inevitable in order to obtain a dense membrane) and, more possibly, the lower magnetic field strength (0.81 T) used in this study compared to Murata's (0.9 T). Therefore, there is still significant potential for improving the oxygen flux of textured NNO membranes via optimization of the magnetic field.

To assess the CO<sub>2</sub>-stability of the NNO membranes, the oxygen fluxes were measured by switching the sweep gas from He to CO<sub>2</sub>. Figure 5b shows that the initial flux decreases from 2.03 mL min<sup>-1</sup> cm<sup>-2</sup> to 1.37 mL min<sup>-1</sup> cm<sup>-2</sup> due to the changed atmosphere. However, the flux did not continue to decrease under CO<sub>2</sub> sweeping; instead, it fluctuated around 1.40 mL min<sup>-1</sup> cm<sup>-2</sup> (at 1223 K) and remained unchanged for at least 120 h. To investigate the stability of the NNO membrane at lower temperatures, the membrane was cooled from 1223 K to 1023 K and operated under an air/CO<sub>2</sub> gradient for 20 h. Together with a new membrane tested under the air/CO<sub>2</sub> gradient at 1023 K for 112 h, the results revealed that, like the flux at 1223 K, it was stable at 1023 K. It was also noticed that the flux during the CO<sub>2</sub> sweeping was lower than during the He sweeping. This phenomenon is also reported for other CO<sub>2</sub>-stable materials and is primarily attributed to CO<sub>2</sub> adsorption on the membrane surface, which strongly inhibits the surface-exchange reaction.<sup>[21]</sup> As indicated in Figure S16a, the flux exhibited a slight decrease upon alternating from He to CO<sub>2</sub> due to the adsorption process, and once switching back to He, it fully recovered to its original level because of CO<sub>2</sub> desorption. Considering that the surface exchange process dominates at lower temperatures and that CO<sub>2</sub> adsorption is

more favorable at low temperatures, the negative impact of CO<sub>2</sub> adsorption on the oxygen flux is expected to be more pronounced at lower temperatures.<sup>[21a,22]</sup> Figure S16b confirms this speculation, showing a decrease in flux of 36.6% at 1023 K and 30.8% at 1223 K, respectively.

The CO<sub>2</sub>-stability of NNO is also proved by XRD as shown in Figure S15. No carbonate was formed in NNO powder after treatments within 1023 K–1223 K for 2 h or at 1023 K from 2 h to 230 h in a pure CO<sub>2</sub> atmosphere. A phase transition from orthorhombic ( $\delta=0.20$ ) to tetragonal ( $\delta=0.08$ ) was observed. Upon reheating the powder (in CO<sub>2</sub> at 1223 K for 96 h) in air, the tetragonal phase returned to the orthorhombic phase within 2 h. The phase transition under different oxygen partial pressures is reasonable, and the influence of oxygen partial pressure on the NNO structure has been well studied.<sup>[23]</sup> The results in Figure S15 indicated excellent CO<sub>2</sub>-stability of NNO. At 1023 K, the CO<sub>2</sub> desorption process is faster than its adsorption process on the surface of NNO. Upon switching to He sweeping, the flux can quickly recover due to the rapid CO<sub>2</sub> desorption (see Figure S16a). The decrease in oxygen flux during CO<sub>2</sub> sweeping is thus attributed to CO<sub>2</sub> adsorption on the membrane surface.

The oxygen permeation properties of various OTMs, including the NNO membranes investigated in this study, were compared in Figure 5c and Figure 5d with respect to the membrane thickness (He sweeping) and stable operating duration (CO<sub>2</sub> sweeping). Detailed data can be found in Table S3. The figures demonstrate that membrane configurations with thinner dense layers, e.g. asymmetric disks or hollow-fibers, exhibit higher flux compared to symmetric disks. From a membrane material perspective, M<sub>HIA</sub>(TM)O<sub>3</sub>-type perovskites typically demonstrate high flux under He sweeping. However, when CO<sub>2</sub> is used as the sweep gas, the flux of these perovskites rapidly decreases due to the formation of carbonates. On the other hand, the Ruddlesden-Popper oxides, to which NNO belongs, exhibit a moderate flux and excellent operational stability. The textured asymmetric NNO membranes achieve oxygen flux higher than other K<sub>2</sub>NiF<sub>4</sub>-type materials and is comparable to M<sub>HIA</sub>(TM)O<sub>3</sub>-type perovskites in case of He sweeping.<sup>[24]</sup> Moreover, thanks to its outstanding CO<sub>2</sub>-stability, it demonstrates the highest performance regarding to the flux and a stable operational duration under CO<sub>2</sub> sweeping to the best of our knowledge.

In conclusion, we have demonstrated the possibility of preparing dense textured asymmetric membranes by using a 0.81 T magnetic field followed by pressing and sintering. This method not only facilitates an oxygen flux equivalent to that of the state-of-the-art perovskite oxides, but also enables mid-temperature oxygen permeation (>823 K, see Figure S17), making it particularly relevant for SOFCs.<sup>[6a,16,25]</sup> We note that the anisotropic transport properties of NNO can be further utilized (see Table S2) by optimizing the preparation process, especially the construction of magnetic field. To fulfill the requirement of 5 mL min<sup>-1</sup> cm<sup>-2</sup> for industrial applications,<sup>[15]</sup> its flux can also be enhanced by controlling the pore structure of the support layer or by expanding the concept to a hollow-fiber configuration.<sup>[26]</sup>

## Acknowledgements

The authors thank Prof. Dr. Motohide Matsuda for his helpful suggestions on constructing the magnetic field, Dipl.-Ing. Lorenz Gerdes for assistance in the pole figures measurements, M.Sc. Hannah Bronner for support in the mercury porosimetry measurements, and M. Sc. Mohamed Rasheed for preparing samples during the early stage of this work. This work was supported by the Deutsche Forschungsgemeinschaft (DFG, German Research Foundation, project number: 435833397). Open Access funding enabled and organized by Projekt DEAL.

## Conflict of Interest

The authors declare no conflict of interest.

## Data Availability Statement

The data that support the findings of this study are available from the corresponding author upon reasonable request.

**Keywords:** Conducting Materials · Magnetic Field · Mixed Ionic Electronic Conducting Membranes · Oxygen Separation · Texture

- [1] a) Y. Lin, S. Fang, D. Su, K. S. Brinkman, F. Chen, *Nat. Commun.* **2015**, *6*, 6824; b) J. Zhu, G. Liu, Z. Liu, Z. Chu, W. Jin, N. Xu, *Adv. Mater.* **2016**, *28*, 3511.
- [2] a) H. Stadler, F. Beggel, M. Habermehl, B. Persigehl, R. Kneer, M. Modigell, P. Jeschke, *Int. J. Greenhouse Gas Control* **2011**, *5*, 7; b) C. Zhang, J. Sunarso, S. Liu, *Chem. Soc. Rev.* **2017**, *46*, 2941; c) W. Y. Liang, Z. W. Cao, G. H. He, J. Caro, H. Q. Jiang, *ACS Sustainable Chem. Eng.* **2017**, *5*, 8657; d) M. Vellini, M. Gambini, *Int. J. Greenhouse Gas Control* **2015**, *36*, 144.
- [3] a) M. A. Peña, J. L. Fierro, *Chem. Rev.* **2001**, *101*, 1981; b) C. Duan, J. Tong, M. Shang, S. Nikodemski, M. Sanders, S. Ricote, A. Almansoori, R. O'Hayre, *Science* **2015**, *349*, 1321; c) S. Sengodan, S. Choi, A. Jun, T. H. Shin, Y.-W. Ju, H. Y. Jeong, J. Shin, J. T. S. Irvine, G. Kim, *Nat. Mater.* **2014**, *14*, 205; d) Y. H. Huang, R. I. Dass, Z. L. Xing, J. B. Goodenough, *Science* **2006**, *312*, 254.
- [4] a) X. Dong, W. Jin, N. Xu, K. Li, *Chem. Commun.* **2011**, *47*, 10886; b) S. H. Morejudo, R. Zanón, S. Escolástico, I. Yuste-Tirados, H. Malerød-Fjeld, P. K. Vestre, W. G. Coors, A. Martínez, T. Norby, J. M. Serra, C. Kjølseth, *Science* **2016**, *353*, 563; c) H. Jiang, H. Wang, F. Liang, S. Werth, T. Schiestel, J. Caro, *Angew. Chem. Int. Ed.* **2009**, *48*, 2983; d) H. Jiang, H. Wang, S. Werth, T. Schiestel, J. Caro, *Angew. Chem. Int. Ed.* **2008**, *47*, 9341.
- [5] P. M. Geffroy, E. Blond, N. Richet, T. Chartier, *Chem. Eng. Sci.* **2017**, *162*, 245.
- [6] a) Z. Shao, W. Yang, Y. Cong, H. Dong, J. Tong, G. Xiong, *J. Membr. Sci.* **2000**, *172*, 177; b) J. Zhu, G. Zhang, G. Liu, Z. Liu, W. Jin, N. Xu, *Adv. Mater.* **2017**, *29*, 1606377; c) M. Li, H. Niu, J. Druce, H. Téllez, T. Ishihara, J. A. Kilner, H. Gasparyan, M. J. Pitcher, W. Xu, J. F. Shin, L. M. Daniels, L. A. H. Jones, V. R. Dhanak, D. Hu, M. Zanella, J. B. Claridge, M. J. Rosseinsky, *Adv. Mater.* **2019**, *32*, 1905200;

- d) M. Arnold, H. Wang, A. Feldhoff, *J. Membr. Sci.* **2007**, 293, 44; e) S. Engels, T. Markus, M. Modigell, L. Singheiser, *J. Membr. Sci.* **2011**, 370, 58.
- [7] T. Klande, O. Ravkina, A. Feldhoff, *J. Membr. Sci.* **2013**, 437, 122.
- [8] a) W. Fang, F. Steinbach, Z. Cao, X. Zhu, A. Feldhoff, *Angew. Chem. Int. Ed.* **2016**, 55, 8648; b) N. Han, C. Zhang, X. Tan, Z. Wang, S. Kawi, S. Liu, *J. Membr. Sci.* **2019**, 587, 117180; c) J. M. Serra, J. Garcia-Fayos, S. Baumann, F. Schulze-Küppers, W. A. Meulenbergh, *J. Membr. Sci.* **2013**, 447, 297.
- [9] a) J. Xue, G. W. Weng, L. Chen, Y. P. Suo, Y. Y. Wei, A. Feldhoff, H. H. Wang, *J. Membr. Sci.* **2019**, 573, 588; b) Y. Wang, H. Hao, J. Jia, D. Yang, X. Hu, *J. Eur. Ceram. Soc.* **2008**, 28, 3125; c) J. H. Joo, K. S. Yun, J. H. Kim, Y. Lee, C. Y. Yoo, J. H. Yu, *ACS Appl. Mater. Interfaces* **2015**, 7, 14699.
- [10] Y. I. Kwon, G. D. Nam, G. Lee, S. Choi, J. H. Joo, *Adv. Energy Sustainability Res.* **2022**, 3, 2200086.
- [11] a) M. Yashima, M. Enoki, T. Wakita, R. Ali, Y. Matsushita, F. Izumi, T. Ishihara, *J. Am. Chem. Soc.* **2008**, 130, 2762; b) M. Yashima, N. Sirikanda, T. Ishihara, *J. Am. Chem. Soc.* **2010**, 132, 2385; c) L. Minervini, R. W. Grimes, J. A. Kilner, K. E. Sickafus, *J. Mater. Chem.* **2000**, 10, 2349; d) E. Boehm, J. M. Bassat, P. Dordor, F. Mauvy, J. C. Grenier, P. Stevens, *Solid State Ionics* **2005**, 176, 2717.
- [12] a) M. Brunelli, M. Coduri, M. Ceretti, W. Paulus, *J. Phys. D* **2015**, 48, 504009; b) A. Perrichon, A. Piovano, M. Boehm, M. Zbiri, M. Johnson, H. Schober, M. Ceretti, W. Paulus, *J. Phys. Chem. C* **2015**, 119, 1557.
- [13] J.-M. Bassat, M. Burriel, O. Wahyudi, R. Castaing, M. Ceretti, P. Veber, I. Weill, A. Villesuzanne, J.-C. Grenier, W. Paulus, J. A. Kilner, *J. Phys. Chem. C* **2013**, 117, 26466.
- [14] a) J. Song, D. Ning, B. Boukamp, J.-M. Bassat, H. J. M. Bouwmeester, *J. Mater. Chem. A* **2020**, 8, 22206; b) E. Y. Pikalova, V. A. Sadykov, E. A. Filonova, N. F. Ereemeev, E. M. Sadovskaia, S. M. Pikalov, N. M. Bogdanovich, J. G. Lyagaeva, A. A. Kolchugin, L. B. Vedmid, A. V. Ishchenko, V. B. Goncharov, *Solid State Ionics* **2019**, 335, 53.
- [15] a) A. Chronos, B. Yildiz, A. Tarancón, D. Parfitt, J. A. Kilner, *Energy Environ. Sci.* **2011**, 4, 2774; b) A. Flura, S. Dru, C. Nicolle, V. Vibhu, S. Fourcade, E. Lebraud, A. Rougier, J.-M. Bassat, J.-C. Grenier, *J. Solid State Chem.* **2015**, 228, 189; c) J. A. Kilner, M. Burriel, *Annu. Rev. Mater. Res.* **2014**, 44, 365.
- [16] A. Murata, T. Uchikoshi, M. Matsuda, *J. Power Sources* **2015**, 293, 95.
- [17] S. R. Maity, M. Ceretti, L. Keller, J. Schefer, B. Roessli, U. Stuhr, C. Niedermayer, W. Paulus, *Phys. Rev. Mater.* **2023**, 7, 024412.
- [18] T. Kimura, T. Uemura, T. Kimura, S. Takagi, H. Inoue, *Macromol. Symp.* **2006**, 242, 120.
- [19] a) T. S. Suzuki, T. Uchikoshi, Y. Sakka, *Sci. Technol. Adv. Mater.* **2006**, 7, 356; b) Z. Yang, J. Yu, C. Li, Y. Zhong, W. Xuan, Z. Ren, Q. Wang, Y. Dai, H. Wang, *Cryst. Res. Technol.* **2015**, 50, 645; c) T. Uchikoshi, T. S. Suzuki, F. Tang, H. Okuyama, Y. Sakka, *Ceram. Int.* **2004**, 30, 1975.
- [20] F. Mauvy, J. M. Bassat, E. Boehm, J. P. Manaud, P. Dordor, J. C. Grenier, *Solid State Ionics* **2003**, 158, 17.
- [21] a) Y. Wei, J. Tang, L. Zhou, J. Xue, Z. Li, H. Wang, *AIChE J.* **2011**, 58, 2856; b) G. Chen, Z. Zhao, M. Widenmeyer, T. Frömling, T. Hellmann, R. Yan, F. Qu, G. Himm, J. P. Hofmann, A. Feldhoff, A. Weidenkaff, *J. Membr. Sci.* **2021**, 639, 119783; c) Z. Zhao, L. Rehder, F. Steinbach, A. Feldhoff, *Membranes* **2022**, 12, 1123.
- [22] H. Luo, K. Efimov, H. Jiang, A. Feldhoff, H. Wang, J. Caro, *Angew. Chem. Int. Ed.* **2010**, 50, 759.
- [23] a) M. Ceretti, O. Wahyudi, G. André, M. Meven, A. Villesuzanne, W. Paulus, *Inorg. Chem.* **2018**, 57, 4657; b) K. Ishikawa, K. Metoki, H. Miyamoto, *J. Solid State Chem.* **2009**, 182, 2096.
- [24] a) B. Gędziorowski, K. Cichy, A. Niemczyk, A. Olszewska, Z. Zhang, S. Kopeć, K. Zheng, M. Marzec, M. Gajewska, Z. Du, H. Zhao, K. Świerczek, *J. Eur. Ceram. Soc.* **2020**, 40, 4056; b) A. Niemczyk, A. Stępień, K. Cichy, J. Dąbrowa, Z. Zhang, B. Gędziorowski, K. Zheng, H. Zhao, K. Świerczek, *J. Solid State Chem.* **2021**, 296, 121982; c) Q. Zheng, J. Xue, Q. Liao, Y. Y. Wei, Z. Li, H. H. Wang, *Chem. Eng. Sci.* **2013**, 101, 240.
- [25] Z. Shao, S. M. Haile, *Nature* **2004**, 431, 170.
- [26] A. Kaiser, S. P. Foghmoes, G. Pečanac, J. Malzbender, C. Chatzichristodoulou, J. A. Glasscock, D. Ramachandran, D. W. Ni, V. Esposito, M. Sjøgaard, P. V. Hendriksen, *J. Membr. Sci.* **2016**, 513, 85.

Manuscript received: August 28, 2023

Accepted manuscript online: November 21, 2023

Version of record online: December 18, 2023